Metasomatized mantle source of nascent oceanic crust in the Guaymas Basin, Gulf of California

Zhen-Min Ge [a,b], Xiao-Long Huang [a,*], Wei Xie [c,*], Tobias W. Höfig [d,1], Fan Yang [e], Yang Yu [a], S. Khogenkumar Singh [f]

[a] State Key Laboratory of Isotope Geochemistry, CAS Center for Excellence in Deep Earth Science, Guangzhou Institute of Geochemistry, Chinese Academy of Sciences, Guangzhou 510640, China
[b] University of Chinese Academy of Sciences, Beijing 100049, China
[c] Key Laboratory of Marine Hazards Forecasting, College of Oceanography, Hohai University, Nanjing 210024, China
[d] International Ocean Discovery Program, Texas A&M University, 1000 Discovery Drive, College Station, TX 77845, USA
[e] Southern Marine Science and Engineering Guangdong Laboratory (Guangzhou), Guangzhou 511458, China
[f] CSIR-National Institute of Oceanography (CSIR-NIO), Goa 403004, India

A B S T R A C T

The geochemical characteristics of nascent oceanic crust play a crucial role in unraveling the mantle dynamics of the initial opening of an ocean. The Gulf of California, located at the East Pacific margin, is one of the best examples of an active and obliquely rifted continental margin. However, the mantle source composition of the nascent oceanic crust in the central part of the Gulf has not yet been comprehensively investigated. Here, we report *in situ* major and trace element contents as well as B—Sr isotope compositions for basaltic glass samples from off-axis sills drilled by the International Ocean Discovery Program (IODP) Expedition 385 at Sites U1547 and U1548 in the Guaymas Basin in the central part of the Gulf of California. These glassy samples represent tholeiites and predominantly show trace element patterns akin to those of enriched mid-ocean ridge basalts (E-MORBs) but with distinctive enrichments in Ba and K and depletions in Nb, Ta, and Ti. In addition, these samples have high B contents (3.07–3.67 ppm) with enriched Sr isotopes ($^{87}Sr/^{86}Sr$ = 0.7032–0.7037) and heavy B isotopes ($\delta^{11}B$ = −5.52‰ to 1.20‰). The mixing model based on B/Nb values and Sr—B isotopes shows that the nascent oceanic crust in the Guaymas Basin might be generated through partial melting of a depleted MORB mantle (DMM) source metasomatized by melts from subducted slab materials referring to partially dehydrated sediment and altered oceanic crust components. The magmas in the Gulf of California show a systematic decline in their enrichment in fluid-mobile elements (Ba) and depletion in fluid-immobile elements (Nb, Ta, and Ti) from the northern (e.g., Isla San Luis volcanic center) to the central part (Guaymas Basin) and southward to the mouth (e.g., Alarcón Basin) of the Gulf. This suggests that the enriched (recycled) components in their mantle source were gradually extracted and exhausted during Gulf opening and oceanic crustal accretion that advanced in a northward direction. Our results indicate that the Guaymas Basin magmas were derived from a mantle that was fertilized by subduction components. The subduction signature corroborates the Gulf opening as a process that started in response to long-term oblique convergence at the eastern Pacific plate margin without any influence from a mantle plume. This evolution is different from nascent ocean basins that evolved from intraplate rifting, such as the Red Sea, leading to vastly different mantle source characteristics.

1. Introduction

The evolution from continental rifting to seafloor spreading and the formation of nascent ocean basins are important early stages of ocean evolution, which is well known as the key part of the "Wilson Cycle" (Wilson, 1966; Wilson et al., 2019). Continental breakup processes are strongly associated with mantle dynamics. When the tension force exceeds the strength of the continental lithosphere, the continental crust

---

breaks up (Dal Zilio et al., 2018), and the upwelling hot mantle further weakens the lithosphere. These processes have been revealed in detail by seismic reflection profiles of continental margins (e.g., Lizarralde et al., 2007; Almalki et al., 2015). However, the geochemical characteristics of nascent oceanic crust are usually unclear because the early-formed slab disappeared by subduction of a mature ocean, especially in the Pacific, which hampers our understanding of mantle dynamics during the initial opening of an ocean.

The Gulf of California, an active oblique rift system at the east Pacific plate margin, is one of the best modern examples of continental lithosphere rupture and transition from rifting to seafloor spreading (Umhoefer, 2011; Wilson et al., 2019). The spreading of the oceanic

crust began at ~7 Ma (Miller and Lizarralde, 2013), shortly after the oblique continental breakup onset at ~12 Ma (Stock and Hodges, 1989; Atwater and Stock, 1998; Oskin et al., 2001; Oskin and Stock, 2003; Vidal-Solano et al., 2008; Busby et al., 2020), suggesting that the lithosphere of the Gulf of California ruptured rapidly. Based on geophysical observations, the principal mechanism for the rapid rupture of the continental lithosphere and opening of the Gulf may have been mantle fertility and possibly crustal structure with a thick sedimentary layer, which enhanced melt extraction (Lizarralde et al., 2007), or oblique divergence across hot and weak lithosphere along a tectonically active margin (Umhoefer, 2011). However, the mantle source composition of the Gulf has not been sufficiently investigated, and hitherto, any
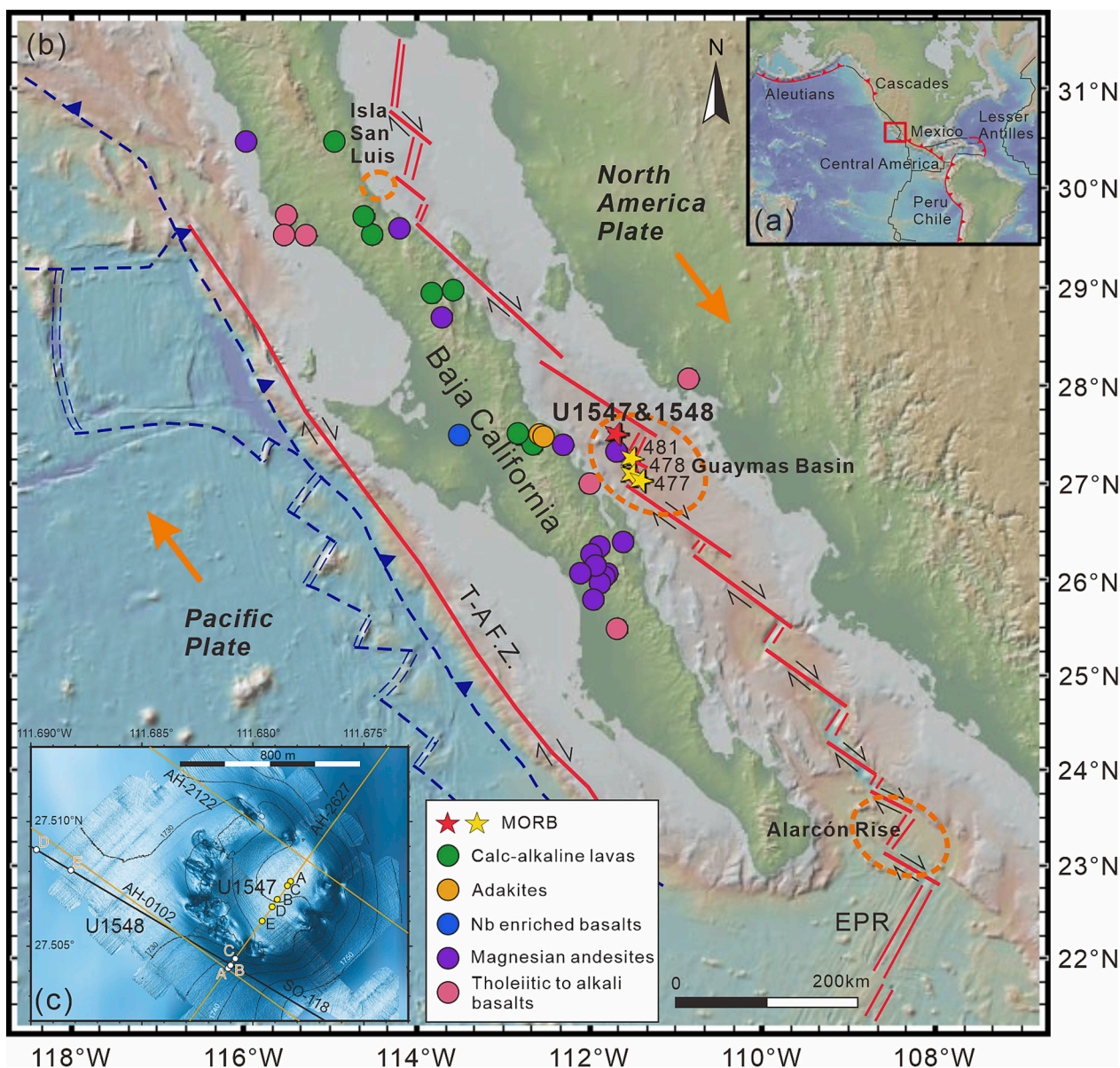
Fig. 1. (a) Tectonic setting of the Gulf of California and the major subduction zones in the area. (b) Topographic map of Baja California and the Gulf of California, showing the distribution of the main onshore basaltic lava types (Rogers et al., 1985; Saunders et al., 1987; Rogers and Saunders, 1989; Martín-Barajas et al., 1995; Aguillón-Robles et al., 2001; Benoit et al., 2002; Calmus et al., 2003; Mora-Klepeis and McDowell, 2004; Conly et al., 2005; Pallares et al., 2007; Nauret et al., 2012; Avellán et al., 2018) and subvolcanic MORB from offshore sites of U1547 and U1548 (IODP Expedition 385; sampled for this study) as well as Sites 477, 478, and 481 (DSDP Leg 64) (Saunders et al., 1982a). The map was made with GeoMapApp 3.6.6 (www.geomapapp.org) (Ryan et al., 2009). T-A F.Z.: Tosco Abreojos Fault Zone, EPR: East Pacific Rise. The red single line indicates an active fault, and the red double line indicates an active spreading center. Blue dashed lines indicate inactive spreading centers, transforms, and trenches. Large orange arrows indicate motion between the Pacific plate and the North American plate. (c) Bathymetric map showing all holes at Sites U1547 and U1548 drilled inside and outside the circular hydrothermal mound structure called Ringvent cited from Teske et al. (2021). Locations of seismic crossing lines are also indicated. Contour lines = 5 m. (For interpretation of the references to colour in this figure legend, the reader is referred to the web version of this article.)

petrologic evidence for the long-term magmatic evolution from rifting to drifting has been derived mainly from on-land lavas (e.g., Busby et al., 2020; Velderrain-Rojas and Vidal-Solano, 2023) that might have been subject to significant crustal contamination. Thus, studies on the actual seafloor spreading center have remained scarce. The Guaymas Basin is in the central part of the Gulf of California and is characterized by active seafloor spreading with on- and off-axis magmas intruding a comparatively thick Quaternary sedimentary overburden (Saunders et al., 1982a, 1982b; Teske et al., 2021). The Guaymas Basin was first drilled by the Deep Sea Drilling Project (DSDP) Leg 64 in 1979/80 (Saunders et al., 1982a). The on-axis hypabyssal igneous rocks (basaltic, doleritic, gabbroic rocks) recovered by that expedition showed slight but noticeable differences (e.g., higher Sr contents) from East Pacific Rise (EPR) MORBs in terms of their geochemical features (Saunders et al., 1982a, 1982b). The geochemical compositions of samples from Guaymas Basin sills may have been influenced by subcontinental material in their mantle source (Saunders et al., 1982a, 1982b; Smith, 1999) or by assimilation of small amounts of sedimentary host material during their emplacement (Verma, 1983).

In 2019, the International Ocean Discovery Program (IODP) Expedition 385 primarily focused on off-axis magmatism, recovering igneous rocks from Sites U1547 and U1548 in the northern off-axis segment of the Guaymas Basin (~27 km northwest of its northern axial graben) (Fig. 1; Teske et al., 2021). In this study, we present *in situ* major and trace element contents (including Cl), Sr isotope ratios, and B contents and isotope ratios for basaltic glassy samples from Site U1547 (Holes U1547C, U1547D, and U1547E) and Site U1548 (Holes U1548A, U1548B, and U1548C) in the Guaymas Basin to investigate the recycled components in their mantle source and elucidate the nature of the nascent igneous oceanic crust. Magmatic glass is generally least affected by shallow differentiation and assimilation processes and thus may effectively reflect the features of the corresponding mantle source. In addition, we assessed the rifting and spreading process and the mantle evolution of the Gulf of California from north to south. Compared with intraplate rifting basins, such as the Red Sea, we reveal that the different nature of the mantle under the Gulf of California may account for their differences in the rifting process and subsequent transition to seafloor spreading without any influence from a mantle plume.

2. Geologic background and sample description

The Gulf of California represents a typical young rifted continental margin between the Baja California Peninsula and western mainland Mexico, occupying the boundary between the Pacific and North American plates (Fig. 1). The spreading system in the Gulf of California includes short seafloor spreading centers offset by long transform faults (Miller and Lizarralde, 2013). The full spreading rate of oceanic crust in the Gulf of California decreases from south to north (47 mm/yr to 43 mm/yr; Plattner et al., 2007).

The Baja California Peninsula represents an extinct subduction zone (Fig. 1) that underwent a significant tectonic shift from oblique convergence to oblique divergence associated with the opening of the Gulf of California (e.g., Calmus et al., 2003; Conly et al., 2005). The Farallon plate (and its present-day remains) has been subducting eastward beneath western North America since the Jurassic period (e.g., Sigloch, 2011). At ~29 Ma, the Pacific–Farallon spreading ridge intersected the North American subduction zone near Baja California, and then two triple junctions were formed and migrated northward and southward (Saunders et al., 1987). The southward migrating triple junction reached the tip of the Baja California Peninsula, and subduction ceased at ~12 Ma (Michaud et al., 2006). Following the cessation of subduction west of the Peninsula, the Gulf of California began to open (Stock and Hodges, 1989; Atwater and Stock, 1998; Oskin et al., 2001; Oskin and Stock, 2003; Vidal-Solano et al., 2008; Busby et al., 2020). The opening initiated a Proto-Gulf phase of rifting (~12 Ma; Stock and Hodges, 1989; Henry and Aranda-Gomez, 2000) and caused the plate

margin to shift from oblique convergence to a transtensional tectonic setting. The onset of seafloor spreading in the Guaymas Basin occurred at ~7 Ma (Miller and Lizarralde, 2013). It makes up the central part of the Gulf and contains two short, NE–SW-trending spreading center segments that are expressed as axial troughs separated by a 20-km-long transform fault (Fig. 1; Saunders et al., 1982a), which is characterized by active seafloor spreading, widespread off-axis magmatism, and rapid sediment deposition (Teske et al., 2021).

The Cenozoic magmatic events in the Gulf of California reflect the complex tectonic evolution of the area. Late Cenozoic calc-alkaline rocks (23–13 Ma) around the Gulf of California (especially the Comondú Formation on Baja California) suggest intermittent subduction of the Farallon Plate (Gastil et al., 1979; Calmus et al., 2011). After ridge-trench collision (13–7 Ma), widespread adakites, Nb-enriched basalts, and magnesian andesites, alongside some tholeiitic, transitional, and alkaline basalts, have been interpreted to reflect the development of a "slab window" beneath northern Baja California (Calmus et al., 2003; Bellon et al., 2006; Pallares et al., 2007, 2008; Castillo, 2008, 2009; Maury et al., 2009). Since ~7 Ma, the Farallon plate has sunk into the deep mantle, and massive tholeiitic, transitional, and alkaline basalts erupted in response to the opening of the Gulf of California and the decompression melting of the asthenosphere (Calmus et al., 2011). In the Guaymas Basin, numerous mafic hypabyssal rocks from several sill intrusions were recovered from Sites U1547 and U1548 of IODP Expedition 385. The two sites are located ~27 km northwest of the axial graben of the northern Guaymas Basin, only a few hundred meters apart from each other (maximum distance between holes = ~800 m) (Fig. 1c; Teske et al., 2021). Holes U1547A–U1547E are located within a circular bathymetric high called the Ringvent mound, which is a bowl-shaped hydrothermal mound that is still active today, and three holes at Site U1548 (U1548A, U1548B, and U1548C) are situated at the periphery of Ringvent's southwestern edge. Mafic hypabyssal rocks were recovered at shallow depths at Sites U1547 (81.5–209.9 m below seafloor, mbsf) and U1548 (64.7–103.0 mbsf). The downhole lithological changes at Sites U1547 and U1548 are not significant enough to necessitate division into more than one igneous lithologic unit. Based on sediment paleomagnetism, all cores at Sites U1547 and U1548 are assigned to ages younger than 0.78 Ma (Teske et al., 2021). The water-rich sediments recovered at Sites U1547 and U1548 are middle to late Pleistocene in age and mostly biogenic (mainly diatom ooze), with a small proportion of siliciclastic components (Teske et al., 2021).

Sills recovered at Site U1547 are predominantly composed of aphyric to clinopyroxene-plagioclase phyric basaltic rock. A doleritic section containing plagioclase and pyroxene phenocrysts (~20 m thick) was recovered from the bottom part of Hole U1547E (down to 191.2 mbsf) (Teske et al., 2021). The basaltic rock is moderately to highly vesicular, while the doleritic intervals are slightly to moderately vesicular. Basaltic rocks recovered at Site U1548 resemble those at Site U1547, but they are darker in colour and usually moderately to highly vesicular. However, at the microscopic scale, aphyric basaltic, sparsely to moderately clinopyroxene-plagioclase phyric basaltic, and plagioclase-clinopyroxene phyric doleritic rocks from Sites U1547 and U1548 show a well-preserved primary igneous mineral assemblage (plagioclase, clinopyroxene, and Fe—Ti oxides) and microtextures (e.g., glomeroporphyritic, subophitic, and intersertal). The igneous rocks from Holes U1547A–U1547E and U1548A–U1548C are cut by sedimentary veins and show contacts between sedimentary breccia and basaltic rock, sediment-magma mingling (peperite facies), and glassy chilled margins (Teske et al., 2021). The samples in this study represent basaltic glass margins from Sites U1547 (Holes U1547C, U1547D, and U1547E) and U1548 (Holes U1548A, U1548B, and U1548C). They are mostly hyaline, containing small amounts of crystals that represent mainly fine-grained plagioclase and clinopyroxene minerals (Fig. 2). The glass formed in response to quenching of magma when it intruded very wet shallow sediments. The sample depth is presented in Table S1 with a range of 67.80–140.00 mbsf.
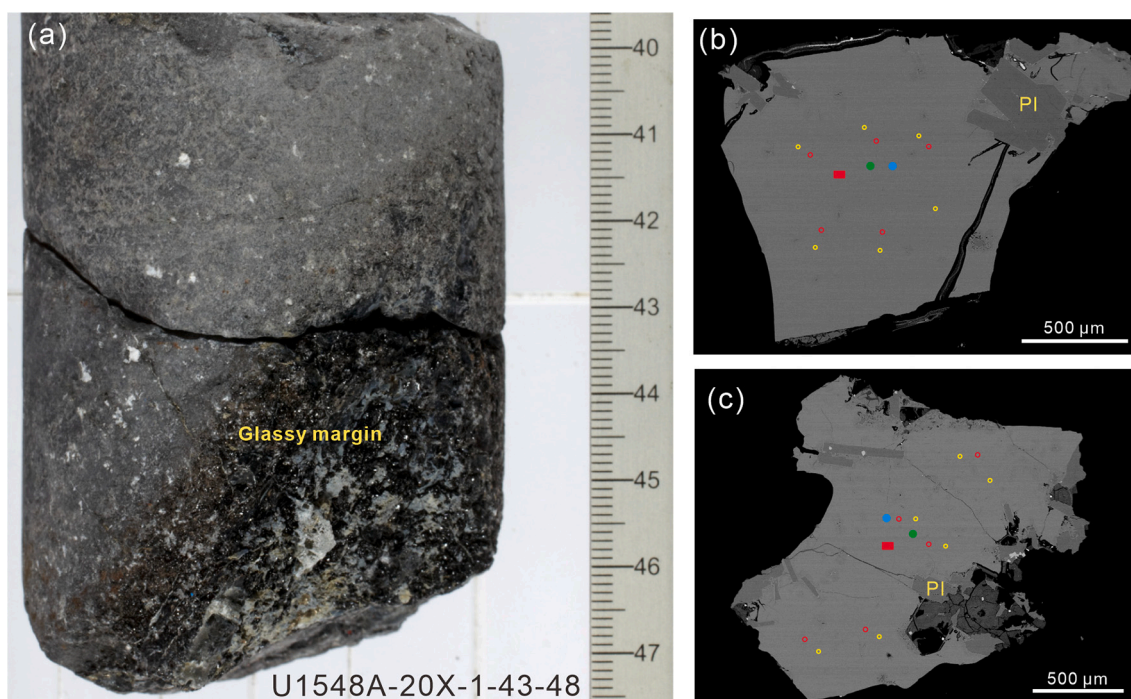
Fig. 2. Representative hand specimen photo (a) and BSE images (b-c) of the glassy samples from Sites U1547 and U1548. (a) Sample U1548A-20X-1-43/48, (b) Sample U1547E-4R-2-36/44, and (c) Sample U1547E-12R-1-20/24. Yellow circles show the locations of EPMA major element analyses and red circles show the locations of Cl element analyses. Blue and green solid dots are locations of LA-ICP-SF-MS trace element analyses and LA-ICP-MC-MS Sr isotope analyses, respectively. Red solid rectangles show the locations of SIMS B isotope analyses. Mineral abbreviations: Pl, plagioclase. (For interpretation of the references to colour in this figure legend, the reader is referred to the web version of this article.)

3. Analytical methods

In situ analyses of major and trace element contents, Sr isotope ratios, B contents and isotope ratios for 12 glassy samples from the Guaymas Basin were performed at the State Key Laboratory of Isotope Geochemistry (SKLaBIG), Guangzhou Institute of Geochemistry, Chinese Academy of Sciences (GIG-CAS), Guangzhou, China (see Table S1 for detailed sample information).

All glassy samples were crushed in an agate mortar to obtain fragments of <2 mm in size. These glass shards were then cleaned in an ultrasonic bath in Milli-Q deionized water and subsequently air-dried. The glassy samples were examined and selected under a binocular microscope based on their fresh appearance. The glass shards were subsequently mounted in an epoxy bonding agent, single polished, and reserved for further measurements.

The contents of major elements (Si, Ti, Al, Fe, Mn, Mg, Ca, Na, K, and P) and Cl were obtained using a Cameca SX Five FE electron probe microanalyzer (EPMA). An operating condition of 15 kV accelerating voltage and 20 nA beam current was used for analysis of major element contents and 15 kV accelerating voltage and 200 nA beam current for analysis of Cl and S contents. The electron beam spot diameter was 15 μm for major elements and 20 μm squared scans for Cl. Calibration standards included albite (Na), plagioclase (Si, Al), olivine (Si, Mg), orthoclase (K), diopside (Ca), $RbTiPO_5$ (P), rutile (Ti), rhodonite (Mn), chromite (Cr), Fe_2O_3 (Fe), tugtupite (Cl) and BHOV-2G (Si, Al, Mg, Ca, Fe). The analysis parameters and detection limits are shown in Table S2, and detailed procedure information refers to He et al. (2021). Each sample was measured in five or six domains, and the results were reported as the average value (Table S1).

In situ trace elements were analyzed by an inductively coupled plasma sector field mass spectrometry (ICP-SF-MS) instrument (ELEMENT XR; Thermo Fisher Scientific, Bremen, Germany) with a laser ablation system (M-50; Resonetics, Nashua, NH, USA) equipped with an ArF excited dimer (excimer) laser (COMPexPro 102; Coherent, Santa

Clara, CA, USA; wavelength, 193 nm). In the laser ablation process, helium was used as a carrier gas. Each spot analysis consisted of 20 s of gas blank collection with the laser switched off and 30 s of sample signal detection with the laser running. The laser diameter was 17–33 μm, and the repetition rate was limited to 4 Hz. The data were processed by an in-house created MATLAB program called TraceElement, using the internal standard method with Si as the internal standard element. TB-1G was used as a reference glass (Table S3), indicating precision from <20% to <8% (2RSD) and accuracy from ±20% to ±10%, as described in Zhang et al. (2019).

Sr isotope analyses were performed on a Neptune Plus MC-ICP-MS (Thermo Scientific) coupled with a RESOlution M-50193 nm laser ablation system (Resonetics). The laser parameters were set as follows: 210 μm beam diameter, 7 Hz repetition rate, and ~ 4 J cm^2 energy density. Each analysis consisted of 250 cycles with an integration time of 0.262 s per cycle, including the first 30 s of background acquisition, followed by 30 s for laser ablation and signal collection with the laser beam switched on. During the measurement, the gas blanks of ^{83}Kr and ^{88}Sr were <2.5 mV and 0.5 mV, respectively. The interferences of ^{84}Kr and ^{86}Kr on ^{84}Sr and ^{86}Sr were corrected by subtracting the gas blank from the raw time-resolved signal intensities. ^{85}Rb was used to correct the interference of ^{87}Rb on ^{87}Sr with a natural $^{85}Rb/^{87}Rb = 2.593$ (Catanzaro et al., 1969). The mass bias of $^{87}Sr/^{86}Sr$ was normalized to $^{87}Sr/^{86}Sr = 0.1194$ with an exponential law. The detailed data reduction procedure is reported in Zhang et al. (2018). NKT-1G was used as a standard sample, and the standard and duplicated analyses are shown in Table S4.

In situ B contents and isotopic compositions were determined using a CAMECA IMS 1280-HR ion microprobe. The primary $^{16}O^{2-}$ ion-beam current was 100 nA and 40 nA with a voltage of 13 kV, the secondary acceleration voltage was 10 kV, the energy window was ±50 eV without offset, and a 60 mm × 60 mm scan was applied during presputtering for 240 s to remove the gold layer and reduce surface contamination. The mass resolution (M/DM) was set to 1500 at 10% intensity, which was

sufficient to resolve potential interferences of $^1H^9Be^+$ and $^1H^{10}B^+$ with $^{10}B^+$ and $^{11}B^+$, respectively. For detailed information, refer to He et al. (2020). The reference material BCR-2G was used as the calibration standard, and GSD-1G was used as the monitor standard (Table S5). ^{28}Si was also measured to obtain the B content calibration curve to calculate the B content. The error of the calibration curve's slope and the analytical uncertainty are propagated to yield the error (2SE, double standard error) of the B content.

4. Results

The geochemical results of glassy samples from Sites U1547 and U1548 in the Guaymas Basin are presented in Table S1. There is a narrow range of major elements (Figs. 3 and 4), indicating a tholeiitic composition (Fig. 3). These samples show major elements within the range of previously reported on-axis basaltic rocks from Sites 477, 478, and 481, with the exception of higher Na_2O contents (3.52–3.64 wt%) (Fig. 4). They also have higher Na_2O and K_2O (0.39–0.48 wt%) and slightly lower CaO/Al_2O_3 (0.67–0.75) at a given SiO_2 or MgO content than the EPR 20–24°N MORBs, with similar FeO^T (9.01–10.3 wt%), Al_2O_3 (14.5–16.4 wt%), and TiO_2 (1.70–2.01 wt%) contents (Fig. 4). Additionally, these samples exhibit consistent Cl concentrations ranging from 241 to 292 ppm (Table S1).

Compared to the on-axis basaltic rocks, the glassy samples from Sites U1547 and U1548 exhibit a more pronounced enrichment (Fig. 5). Their light rare earth elements (LREEs) are enriched with $(La/Sm)_N$ ranging from 1.12 to 1.36 (Table S1), showing similar trace element patterns that resemble E-MORBs on the chondrite-normalized REE and primitive mantle-normalized multi-element diagrams (Fig. 5). However, compared to typical E-MORB, the studied glassy samples exhibit positive Ba and K and negative Nb, Ta, and Ti anomalies on primitive mantle-normalized multi-element diagrams (Fig. 5b). These samples show overall slight Nb—Ta depletion and large ion lithophile element (LILE) enrichment compared to island-arc basalts, resembling back-arc basin basalts (BABBs) (Fig. 5b). Most of these samples exhibit a limited range of trace elements, except for Sample U1547C-7R-1-20/24, which displays especially high concentrations of most trace elements (Fig. 5).

The $^{87}Sr/^{86}Sr$ ratios vary from 0.7032 to 0.7037 with an average of 0.7034 (Table S1) and are more radiogenic than both N- and E-MORB and published Sr isotopes ($^{87}Sr/^{86}Sr$ = 0.7025–0.7029) of sill samples from DSDP Leg 64 Sites 477, 478 and 481 in the Guaymas Basin (Fig. 1b; Smith, 1999). Boron contents (3.07–3.67 ppm) are relatively homogenous, except for Samples U1547C-7R-1-20/24 and U1548A-20X-1-43/48, which display slightly elevated B contents (Table S1 and Fig. 6). In contrast, $\delta^{11}B$ values are quite variable, ranging from −5.52‰ to 1.2‰ (Table S1). Both B contents and $\delta^{11}B$ values are higher than those of fresh MORBs (Fig. 6).

5. Discussion

5.1. Evaluating the influence of seawater and/or hydrothermal alteration

In the Guaymas Basin, numerous off-axis sills intrude organic-rich, predominantly diatomaceous sediments, provide multiple transient heat sources and drive syn- and post-emplacement hydrothermal circulation (Teske et al., 2019, 2021). Thus, it is necessary to evaluate the influence of (seawater- or porewater-derived) hydrothermal fluids on the primary magmatic glass composition before discussing the mantle source and melting conditions.

Assimilation of seawater or a component ultimately derived from seawater is usually recognized by excess chlorine (Cl) (Bischoff and Pitzer, 1985; Zhang et al., 2017). Cl excess in magma is best observed by the use of ratios of Cl against elements of similar magmatic incompatibility, such as potassium (K) or niobium (Nb) because the ratios would not be strongly influenced by fractional crystallization or partial melting but would increase due to the addition of even small amounts of seawater-derived components with high Cl contents relative to K or Nb (e.g., Michael and Schilling, 1989; Kent et al., 1999; Sun et al., 2007; Marschall et al., 2017). The glassy samples from the Guaymas Basin mainly show relatively low Cl contents (242–292 ppm), within the range of E-MORB Cl contents (<600 ppm; Michael and Schilling, 1989), as well as Cl/K values within the range of fresh E-MORB (Fig. 7a), indicating that contamination by seawater (or porewater) should be negligible.

The hydrothermal fluids in the Guaymas Basin are rich in methane and dissolved inorganic carbon, potentially contributing to the formation of hydrothermal carbonate (Teske et al., 2019). Additionally, CaO will leach from the glass into seawater during the initial palagonitization (e.g., Prause et al., 2022). Therefore, CaO contents in hydrothermally altered glass will deviate from the magma differentiation trend. However, the twelve glassy samples from Sites U1547 and U1548 show uniform CaO contents within the range of fresh MORB at a given MgO content (Fig. 7b), indicating that the impact of hydrothermal fluid, if it exists, should be insignificant. The glassy samples in this study barely contain any sulfides (Fig. 2), and their major elements (including Cl) show little variation among different domains, which also suggests that
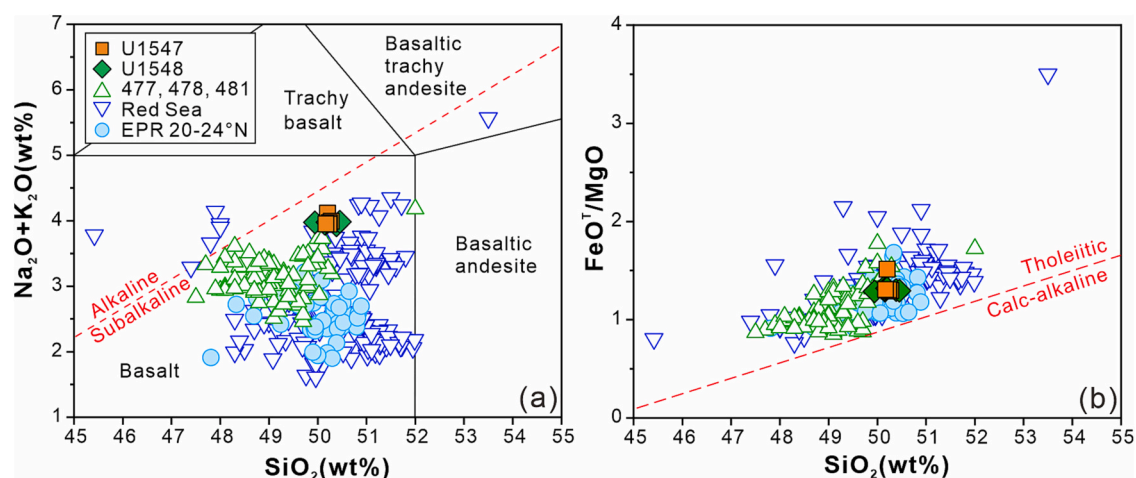

Fig. 3. SiO_2 versus (a) $Na_2O + K_2O$ (total alkali silica plot; in wt%) and (b) FeO^T/MgO for subvolcanic glasses at Sites U1547 and U1548. Sources of data for comparison: basaltic rocks at Sites 477, 478, and 481 from Saunders et al. (1982a); Red Sea glassy samples from van der Zwan et al. (2015) and EPR 20–24°N MORBs compiled and reported in Yang et al. (2021). (For interpretation of the references to colour in this figure legend, the reader is referred to the web version of this article.)
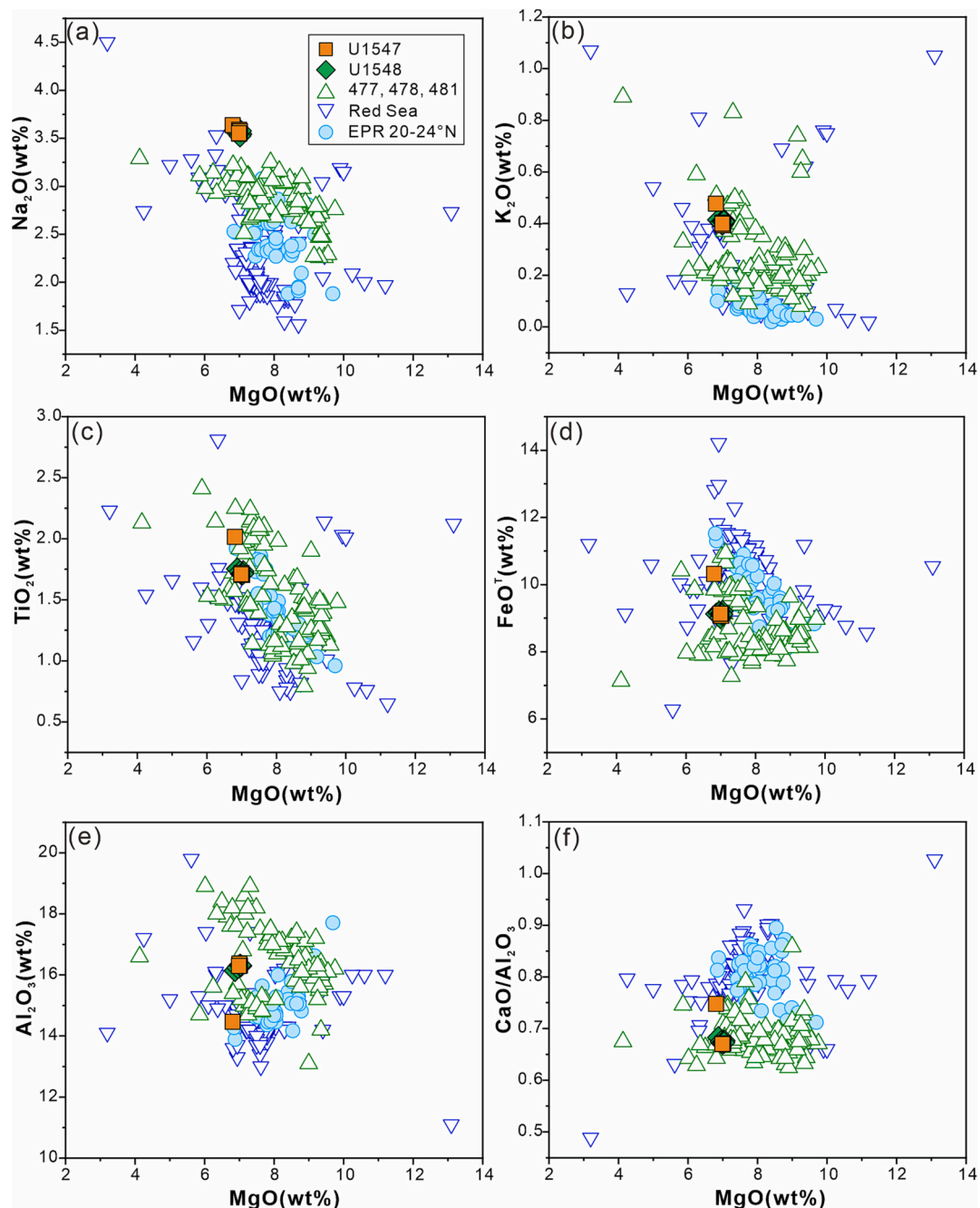
Fig. 4. MgO content (in wt%) versus concentrations of major element oxides (a-e) and CaO/Al$_2$O$_3$ value (f) for subvolcanic glasses from Sites U1547 and U1548. Sources of data for comparison are the same as in Fig. 3.

they are very uniform and that the influence of seawater and/or hydrothermal alteration should be negligible overall.

5.2. Mantle source composition

The basaltic samples of this study display similar chondrite-normalized REE patterns slightly enriched in LREEs and negative Pb anomalies on primitive mantle-normalized multi-element diagrams, resembling those of E-MORBs. However, compared to typical E-MORB, they are selectively enriched in some large ion lithophile elements (LILEs; e.g., Rb, Sr, and K) and depleted in high field strength elements (HFSEs; e.g., Nb, Ta, and Ti) (Fig. 5), which is akin to island-arc and back-arc basin igneous rocks (Hawkesworth et al., 1993; Schmidt and Jagoutz, 2017; Rustioni et al., 2021; Li et al., 2022). In addition, these

basaltic glassy samples show much lower Ce/Pb and Nb/U values than those of the depleted mantle and plot straddling the two fields of MORB and BABB on the diagram of Ce/Pb vs. Nb/U (Fig. 8). These observations suggest that the present-day mantle source might have been affected by subducted components prior to rift- and spreading-related decompression melting. The Guaymas Basin is an active spreading center, suggesting that such geochemical features should be inherited from pre-Gulf stage processes likely related to Farallon plate subduction (e.g., metasomatism by slab-derived components or recycled crustal material).

A subducting slab can influence the mantle source by introducing subducted sediments and altered oceanic crust (AOC), leading to metasomatism in the mantle wedge. The components derived from the slab can exist as fluid and melt, displaying distinct mobilities for
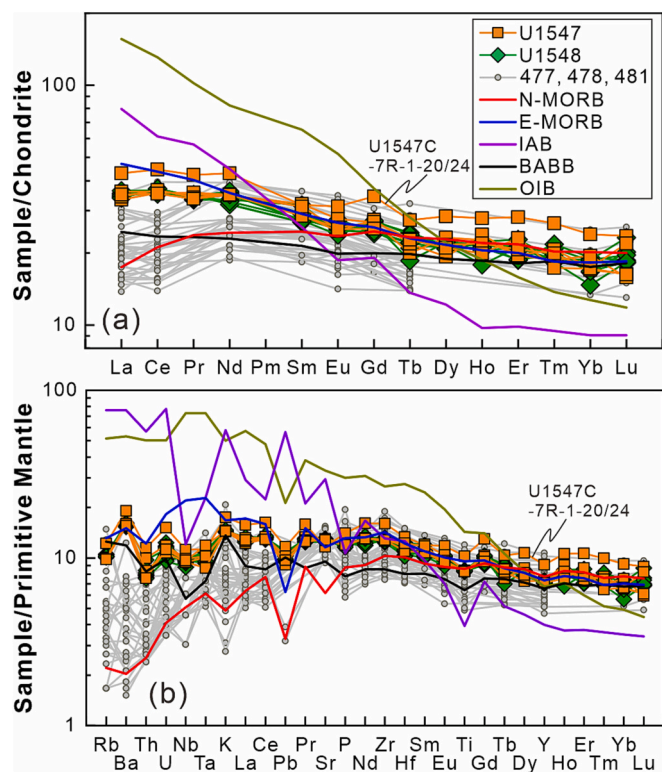
Fig. 5. (a) C1 chondrite-normalized rare-earth element (REE) distribution diagram and (b) primitive mantle-normalized multielement diagram for the glassy samples from Sites U1547 and U1548. Basaltic rocks at Sites 477, 478, and 481 are from Saunders et al. (1982a). C1 chondrite normalization values are from Sun and McDonough (1989), and primitive mantle normalization values are from Mcdonough and Sun (1995). Normal mid-ocean ridge basalt (N-MORB), enriched mid-ocean ridge basalt (E-MORB), and ocean island basalt (OIB) data are from Niu and O'Hara (2003); back-arc basin basalt (BABB) data are from White and Klein (2014) and island arc basalt (IAB) data are from Kelemen et al. (2014).
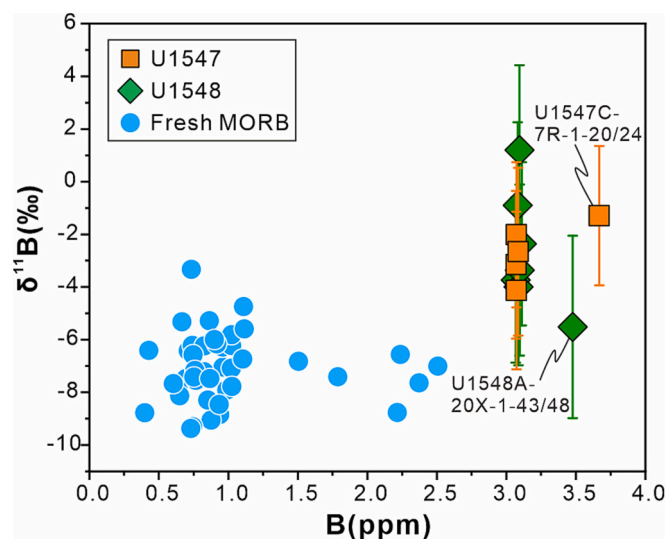

Fig. 6. Boron (B) content versus $\delta^{11}B$ of glasses from Sites U1547 and U1548. Reference data for fresh MORB (Cl/K<0.08) are from Marschall et al. (2017).

different elements (e.g., Kessel et al., 2005; Ni et al., 2017). Different subduction components might be well distinguished by Sr isotopes and stable isotopes such as B isotopes (e.g., Yu et al., 2021). Boron is a fluid-

mobile element and is highly incompatible in magmatic systems (e.g., De Hoog and Savov, 2018). Boron has two stable isotopes, i.e., [10]B and [11]B. [11]B preferentially occupies trigonal coordination sites in fluid phases, while [10]B likely retains tetrahedral coordination sites in melts (e. g., Spivack and Edmond, 1987; Benton et al., 2001; Hervig et al., 2002). The mantle has low B contents (B < 0.1 ppm; Ryan et al., 1996; Ishikawa and Tera, 1999; Pabst et al., 2012; Marschall et al., 2017) with low $\delta^{11}B$ values (−7 ± 2‰) resembling those of MORBs (−7.1 ± 0.9‰; Marschall et al., 2017). However, seawater has a high B content (~4.4 ppm) and shows an extremely heavy B isotope composition ($\delta^{11}B$ = +39.6‰; Foster et al., 2010). Sediments, AOC, and serpentinized lithosphere are all enriched in B but show distinct B isotope ratios due to seawater influence (Ishikawa and Nakamura, 1994; Benton et al., 2001; Bebout and Nakamura, 2003). In addition, during subduction, sediments and AOC lose B, and the $\delta^{11}B$ values are fractionated by progressive slab dehydration (Scambelluri et al., 2004; Marschall et al., 2007; Konrad-Schmolke and Halama, 2014). Beneath forearcs and volcanic arcs, boron from subducting sedimentary rocks and altered oceanic crust (mainly hosted by micas) is either removed from subduction zone rocks via metamorphic fluids or sequestered by growing secondary minerals such as tourmaline, in which B can be entrained to even greater depths (Bebout and Nakamura, 2003). Seafloor serpentinites show a large range of heavy B isotope compositions with $\delta^{11}B$ values of approximately +5‰ to +40‰ and have high B contents of up to 90 ppm (De Hoog and Savov, 2018). As a result, the fluid originating from the dehydration of serpentinite has a much higher B content due to the low B solid/fluid partition coefficient (~0.11; Kessel et al., 2005). Thus, small amounts of fluids derived from subducted serpentinite through dehydration can significantly influence the B isotope compositions of melts. Because the $\delta^{11}B$ values (−5.52‰ to +1.20‰) of the glassy samples from the Guaymas Basin are much lower than those of serpentinites, their mantle source most likely did not have serpentinite-derived fluids as the major metasomatizing subduction-related component. Therefore, we prefer to consider the partly dehydrated sediments and AOC.

The basaltic samples from the Guaymas Basin, inclusive of Sites U1547 and U1548 in this study, and the on-axis sills from DSDP Sites 477, 478, and 481, show tholeiitic chemistry and major elements (excluding Na$_2$O) that are generally consistent with those of normal MORB from EPR 20–24°N (Figs. 3 and 4). This similarity suggests their derivation from the partial melting of a depleted MORB mantle (DMM). In such a scenario, the depleted mantle source might have interacted with components derived from partly dehydrated sediments and AOC. The glassy samples of the Guaymas Basin show slightly higher $^{87}Sr/^{86}Sr$, $\delta^{11}B$, and B/Nb values than MORBs and are similar to some basalts from the Cascades arc and some BABBs (Fig. 9). The model calculation based on $^{87}Sr/^{86}Sr$, $\delta^{11}B$, and B/Nb shows that the input of small amounts (~0.02–0.5%) of partly dehydrated sediments and AOC melts into a depleted mantle source can reproduce the compositional characteristics of basaltic glassy samples from the Guaymas Basin (Fig. 9).

It is noteworthy that Sample U1548A-20X-1-43/48 has a high B content and B/Nb value, but exhibits relatively low $\delta^{11}B$ value in our data set (Table. S1). Generally, marine sediments have significantly higher B concentrations (~61.1 ppm; Plank, 2014) and lower $\delta^{11}B$ values (−6.6 to +4.8‰; Ishikawa and Nakamura, 1993) compared to AOC (B = ~26 ppm and $\delta^{11}B$ = ~5.5‰; Leeman et al., 2004). Thus, we propose that the mantle source of this sample might be primarily influenced by sediment (~0.02–0.05%) rather than AOC (Fig. 9). Samples from Sites U1547 and U1548 exhibit higher Na$_2$O contents (Fig. 4a) and show trace element patterns that are more abundant than those from on-axis sills at DSDP Sites 477, 478, and 481 (Fig. 5). This might be attributed to the decrease in the degree of melting. The elevated B content in Sample U1547C-7R-1-20/24 could also be attributed to its low degree of partial melting. This is supported by the fact that this sample exhibits the highest Ce content and (La/Sm)$_N$ (Table. S1), and its B/Nb value is within the range of other samples (Fig. 9a).

Although B in the subducting slab is mostly released during low-
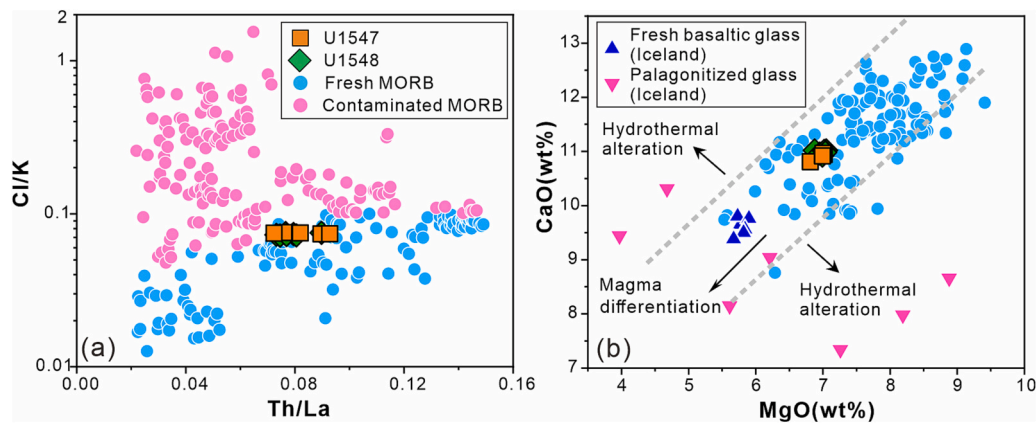
Fig. 7. Plots of (a) Cl/K vs. Th/La and (b) CaO (wt%) vs. MgO (wt%) contents for the glassy samples from Sites U1547 and U1548. The Th/La of the samples can be used as a proxy for long-term geochemical enrichment/depletion of the mantle source, and samples are divided into D-MORB (Th/La ≤ 0.035), N-MORB (0.035 < Th/La < 0.07), and E-MORB (Th/La ≥ 0.07) (Shimizu et al., 2016). D-MORB samples with Cl/K > 0.04, N-MORB samples with Cl/K > 0.06, and E-MORB samples with Cl/K > 0.1 are suggested to be uncontaminated (Shimizu et al., 2016). Data on MORBs in (a-b) are from Shimizu et al. (2016) and Reekie et al. (2019), and data for fresh basaltic glass and palagonitized glass in (b) are from Prause et al. (2022).
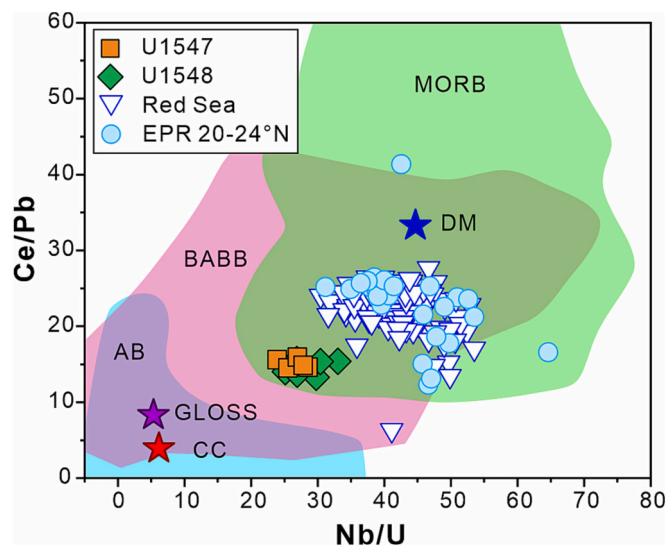
Fig. 8. Plots of (a) Ce/Pb vs. Nb/U for Sites U1547 and U1548 glasses compared with the Red Sea of van der Zwan et al. (2015). The green, pink, and blue regions delineate the respective distribution ranges of mid-ocean ridge basalt (MORB), back-arc basin basalt (BABB), and arc basalt (AB), while the shadow fields represent the intersection region between two adjacent areas. Data for EPR 20–24°N MORBs are from the same literature as in Fig. 3. The endmember of the continental crust (CC) is from Rudnick and Gao (2014), depleted mantle (DM) is from Salters and Stracke (2004) and global subducting sediment (GLOSS) is from Plank and Langmuir (1998). The fields of MORB, BABB, and AB from Yang et al. (2021) are also shown. (For interpretation of the references to colour in this figure legend, the reader is referred to the web version of this article.)

temperature dehydration in the early stage of subduction (Leeman et al., 2004; Tonarini et al., 2007), the subducted material (e.g., liquid from subducted sediments and AOC) is preserved in the mantle (Shaw et al., 2012) and still affects the mantle source of the active spreading center in the Guaymas Basin by hydrous melts. The heavy B isotopic composition originated mainly from partly dehydrated AOC (Fig. 9). In particular, some samples from Site U1548 exhibit higher $\delta^{11}B$ values (Figs. 6 and 9) and Nb/U values (Fig. 8), likely due to more influence of AOC. On the other hand, the enriched Sr isotopic composition may be influenced by recycled sediments (Fig. 9). The samples from Site U1547 display more scattered $^{87}Sr/^{86}Sr$ values (Fig. 9b) and could be affected by diverse

extents of subducted sediments. It is noteworthy that Site U1547 is situated within the Ringvent hydrothermal mound, while Site U1548 is positioned at the periphery of the southwestern edge of Ringvent (Fig. 1c). As the isotope fractionation of B usually exhibits a downward trend with increasing temperature (Kowalski and Wunder, 2018), samples from Site U1548 should display more scattered $\delta^{11}B$ values than those from Site U1547.

5.3. Geochemical evolution during the opening of the Gulf of California

The igneous rocks in the Gulf of California and surrounding areas may represent magmatism at different evolutionary stages from continental rifting to seafloor spreading, including the Baja California and Sonora margin areas (e.g., Paz Moreno and Demant, 1999; Busby et al., 2020; Velderrain-Rojas and Vidal-Solano, 2023). The rift-related basaltic andesites to rhyolites might have been influenced by subduction components in the source and the assimilation of crustal materials at shallow depths (Martín-Barajas et al., 1995; Paz Moreno and Demant, 1999; Conly et al., 2005). For instance, the late Quaternary Isla San Luis volcanic center in the northern Gulf of California (Fig. 1b) sits on top of a thicker lithosphere than the central Gulf area, such as the Guaymas Basin, where the crust has been largely stretched and thinned (Paz Moreno and Demant, 1999). Consequently, more asthenospheric mantle but less crustal assimilation is evident for igneous rocks in the Guaymas Basin. Indeed, the glassy samples from the Guaymas Basin show much weaker anomalies in Ba, Nb, and Ti than the lavas in the Isla San Luis volcanic center (Fig. 10a). However, the lavas in the Alarcón Basin (0–1.5 Ma) at the mouth of the Gulf (Fig. 1b) are MORBs resembling Pacific N-MORB composition (Fig. 10a) without any significant contamination of the continental crust or subduction component (Castillo et al., 2002). This is likely attributed to the homogenization of the mantle source during the early stage of back-arc rifting in a continental environment or the prevalence of a mantle source similar to that of Pacific MORBs (Castillo et al., 2002).

Therefore, the abundance of recycled components in the mantle source of Quaternary igneous rocks exhibits a gradual decline from the northern (Isla San Luis volcanic center) to the central (Guaymas Basin) and southern (Alarcón Basin) parts of the Gulf (Fig. 10b), suggesting that (1) rifting takes place asynchronously, reflecting different stages of basin opening, and (2) the enriched component in the mantle has been purged gradually through melt extraction and accretion of the oceanic crust. Indeed, enriched recycled material is more fertile and preferentially melts compared to depleted mantle (e.g., Sanfilippo et al., 2021) and is gradually extracted and exhausted in the melt extraction process, which
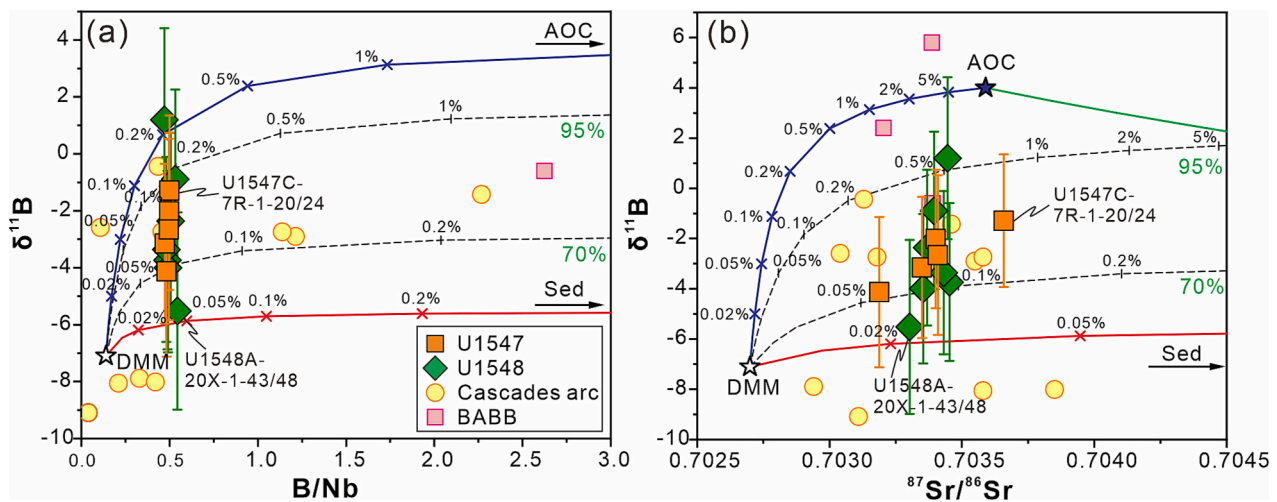
Fig. 9. Diagrams of (a) δ¹¹B vs. B/Nb and (b) δ¹¹B vs. ⁸⁷Sr/⁸⁶Sr for the glasses at Sites U1547 and U1548. Dehydration and hydrous melting conditions and modeling parameters for the sediments (Sed) and altered oceanic crust (AOC) and the depleted MORB mantle (DMM) are summarized in Table S6. Data for the Manus back-arc basin basalts (BABBs) (Shaw et al., 2012) and Cascades arc basalts (Leeman et al., 2004) are also shown, except for some high B/Nb BABB samples in (a). The mixing between DMM and melts from AOC or Sed is shown by the blue and red lines with cross marks, respectively, while the green line denotes the mixing between AOC and Sed-derived melts. The black numbers adjacent to the cross marks indicate the proportion of AOC or Sed-derived melts. The green numbers display the proportion of AOC-derived melts combined with Sed-derived melt. The gray dotted lines with tick marks delineate the metasomatism of the DMM induced by ROC and Sed-derived melts in varying proportions. The black numbers near the tick marks highlight the proportion of the mixed melts. (For interpretation of the references to colour in this figure legend, the reader is referred to the web version of this article.)
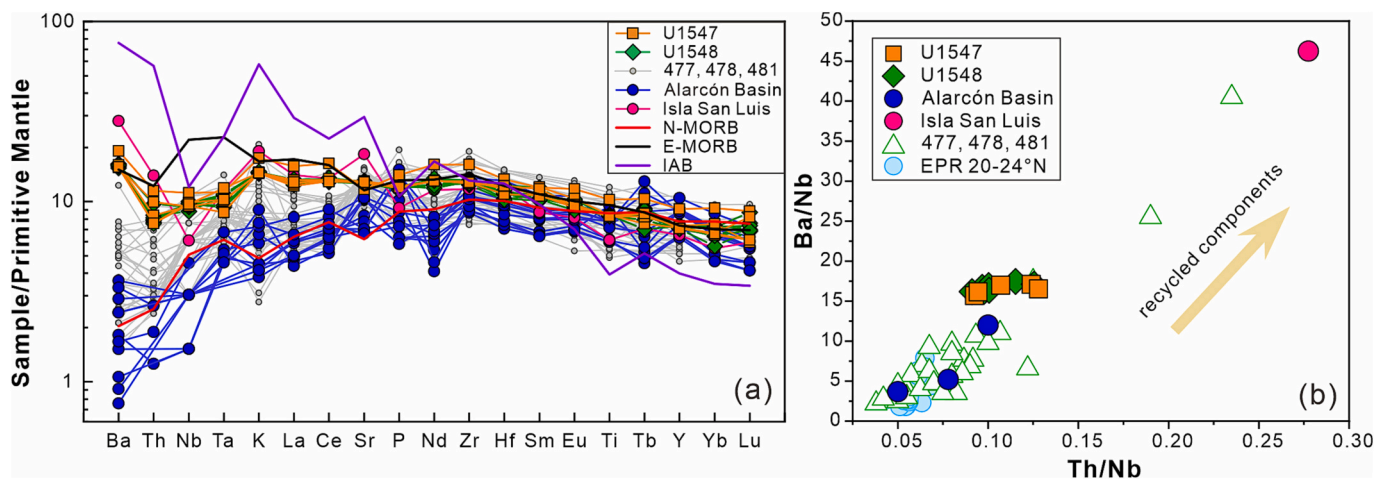

Fig. 10. (a) Primitive mantle-normalized trace element patterns and (b) plot of Ba/Nb vs. Th/Nb for basaltic glasses from Sites U1547 and U1548 compared with basaltic andesite sample 94–31 from the Isla San Luis volcanic center (Paz Moreno and Demant, 1999) and lava samples from the Alarcón Basin (Castillo et al., 2002). Primitive mantle normalization values and reference data for normal mid-ocean ridge basalt (N-MORB), enriched mid-ocean ridge basalt (E-MORB), and island arc basalt (IAB) in (a) are from the same literatures as in Fig. 5. The data for basaltic rocks at Sites 477, 478, and 481, as well as for MORBs at EPR 20–24°N in (b) are from the same literatures as Fig. 3.

provides geochemical evidence for this geophysics-based observation of rapid rift and ocean spreading in a highly oblique-divergent setting (Umhoefer, 2011). This gradual melt extraction process ranging from more fertile to less fertile mantle source rocks reflects the present-day spatial geochemical pattern of igneous rocks from north to south and may reflect a temporal pattern of less to more advanced stages of basin opening and, thus, oceanic crust formation at a given location in the Gulf. During long-lived subduction of the Farallon Plate (Gastil et al., 1979; Calmus et al., 2011) before rifting of the continental crust, the subducted slab progressively dehydrated, and the subcontinental lithospheric mantle was metasomatized by fluids and melts derived from subducted slabs (Fig. 11a). After that, the Farallon plate likely broke off during the sinking and detachment of the deep part of the subducting slab (Schmid et al., 2002; Pallares et al., 2007, 2008; Castillo, 2008;

Zhang et al., 2009) and subsequent upwelling of the asthenosphere. Beneath the largely stretched and thinned continental crust and lithospheric mantle, depleted asthenospheric mantle, which carries recycled, partly dehydrated oceanic crust and sediments, ascends and partially melts to produce igneous rocks with the geochemical features of the glassy Guaymas Basin samples studied, i.e., enrichment in LILEs, LREEs and U but depletion in HFSEs with more radiogenic ⁸⁷Sr/⁸⁶Sr and high δ¹¹B values (Fig. 11b).

5.4. Implications for the evolutionary pathways of young ocean basins

Along the same plate boundaries, ocean basins will repeat opening and closing, which is well known as the "Wilson Cycle", usually including six simplified stages (Wilson et al., 2019 and references
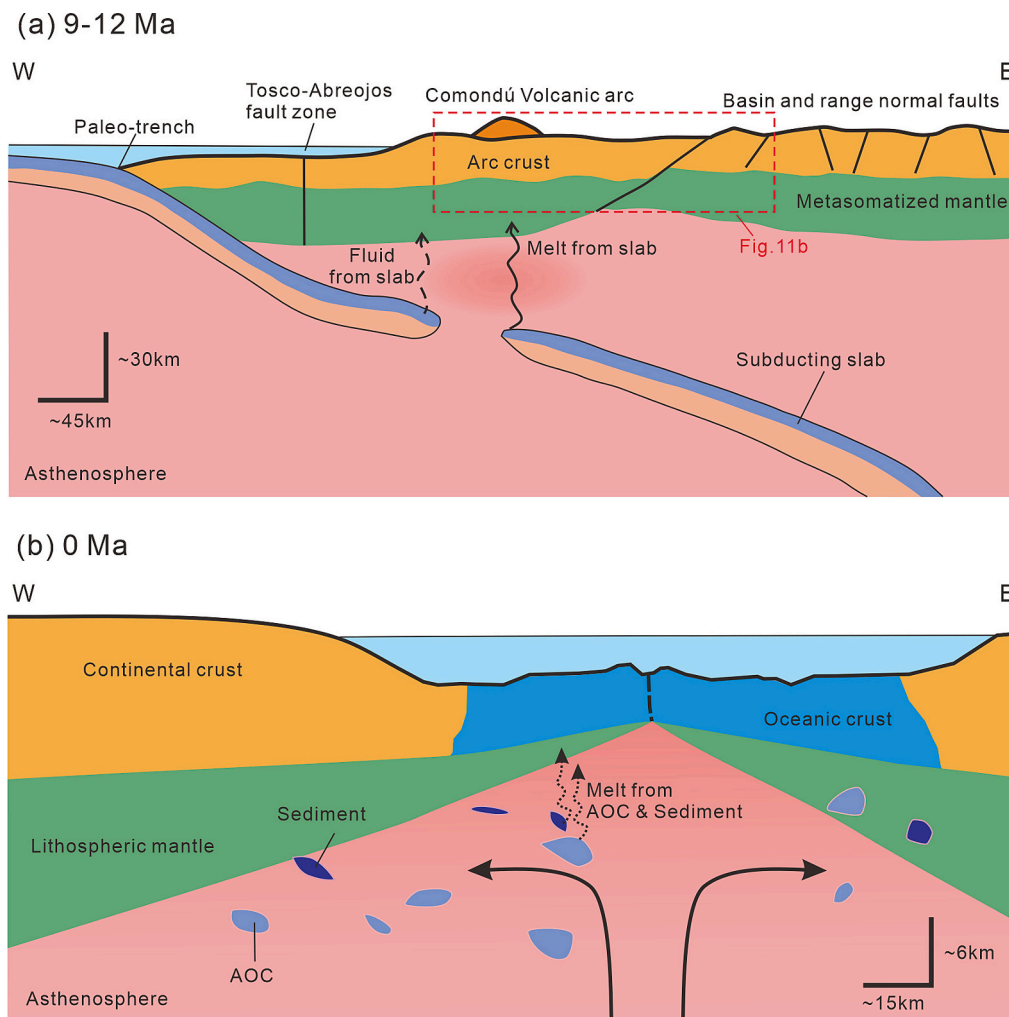
Fig. 11. Schematic W–E cross sections of the Guaymas Basin area at two different time slices (a: 12–9 Ma, and b: 0 Ma), highlighting the mantle source components and the formation of the Guaymas Basin MORB (modified from Castillo, 2008; Calmus et al., 2011). AOC: altered oceanic crust.

therein): (i) the breakup of a continent by rifting; (ii) seafloor spreading and the formation of a nascent ocean; (iii) the formation of a mature ocean; (iv) onset of oceanic subduction and decline; (v) continued oceanic lithosphere subduction and the closure of the ocean basin; and (vi) continent–continent collision. Young rifted continental (passive) margins include thermal subsidence and horizontal extension, such as the Red Sea, Gulf of Aden, and Gulf of California (Wilson et al., 2019). Both the Gulf of California and the Red Sea are typical nascent oceans, but they have undergone distinct processes from continental rifting to seafloor spreading due to different tectonic settings and interactions between structural and magmatic processes.

The Red Sea is an oceanic rift at a divergent plate boundary with a triple junction located in the Afar Depression (Bosworth, 2015). The rifting of the continent in the Red Sea region began at ~8–12 Ma (Augustin et al., 2014; Girdler, 1991; Izzeldin, 1987), and the oldest basalts (~5 Ma) in the south-central Red Sea axial trough (17°N) represent the earliest oceanic crust (Cochran, 1983; Courtillot, 1982). Overall, the Red Sea is an ultraslow to slow-spreading ridge with a full spreading rate of <16 mm/yr (Chu and Gordon, 1998). Indeed, seismic reflection profiles across the Thetis Deep in the Red Sea suggest the presence of a deep magma chamber or melt lens, with the roof lying ~3.2 km below the seafloor, which is deeper than most identified beneath mid-ocean ridges (Ligi et al., 2018). The Gulf of California also underwent a rapid evolution from continental rifting (~12 Ma) to seafloor spreading (~6 Ma) (Umhoefer, 2011), resembling the Red Sea in

temporal terms but showing an intermediate full spreading rate of oceanic crust formation (43–47 mm/yr; Plattner et al., 2007). The magma supply at mid-ocean ridge is related with the thermal structure beneath spreading centers, which in turn, is influenced by factors such as spreading rate, hydrothermal circulation efficiency, and the effectiveness of conductive cooling in heat removal (e.g., Morgan and Chen, 1993; Liu et al., 2022). Thus, there may be larger, long-lived magma reservoirs under the Guaymas Basin compared to the Red Sea.

Trace element patterns of the Red Sea Ridge (between 25.5°N and 16.5°N) basaltic samples range from N-MORB to E-MORB (Fig. 12a), and they show Nb/Yb and Th/Yb ratios plotting within the N-MORB to OIB array (Fig. 12b), suggesting that they lack any characteristics of input of continental materials and are consistent with the interaction of a mantle plume (Afar plume) with the depleted asthenosphere (Altherr et al., 1988; Altherr et al., 1990; Haase et al., 2000; van der Zwan et al., 2015). Indeed, the evolution of the Red Sea is likely driven by both the process of far-field tectonic forces related to the inception of Zagros subduction for ~30–20 Ma and the activity of the Afar plume during 20–15 Ma (Ebinger and Sleep, 1998; Bosworth, 2015; Ligi et al., 2015, 2018). In contrast, in the Guaymas Basin, long-term subduction input of metasomatic deep mantle before rifting and asthenospheric upwelling during the opening of the Gulf by oblique faulting tends to bring up recycled components from the deep mantle that contribute to active magmatic activity without the influence of a mantle plume.
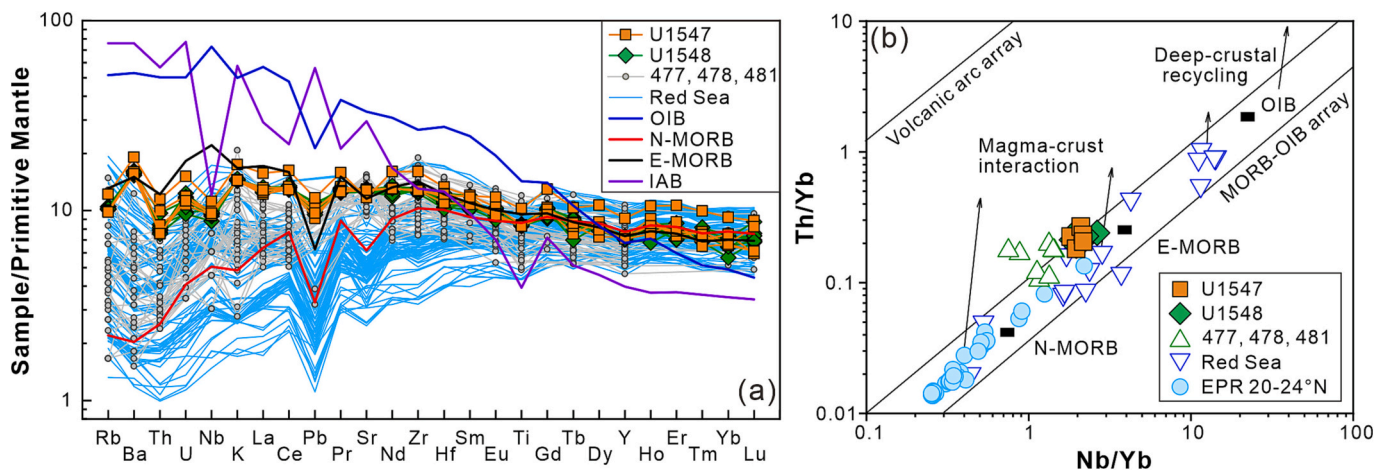
Fig. 12. (a) Primitive mantle-normalized trace element patterns and (b) diagram of Th/Yb vs. Nb/Yb (after Pearce, 2008) for basaltic glasses from Sites U1547 and U1548 compared with those from the Red Sea of van der Zwan et al. (2015). Primitive mantle normalization values and reference data for normal mid-ocean ridge basalt (N-MORB), enriched mid-ocean ridge basalt (E-MORB), ocean island basalt (OIB), and island arc basalt (IAB) in (a) are from the same literatures as in Fig. 5. Data for basaltic rocks at Sites 477, 478, and 481, as well as for MORBs at EPR 20–24°N in (b) are from the same literatures as Fig. 3. (For interpretation of the references to colour in this figure legend, the reader is referred to the web version of this article.)

6. Conclusions

(1) Tholeiitic basaltic glasses from the shallow off-axis Ringvent sill intrusions in Guaymas Basin show trace element characteristics similar to those of E-MORB, but they are enriched in Ba and K while depleted in Nb, Ta, and Ti.

(2) The glasses exhibit higher B contents (3.07–3.67 ppm), $\delta^{11}B$ values (−5.52–1.2 ‰), and $^{87}Sr/^{86}Sr$ isotope ratios (0.7032–0.7037) than MORB. This can be attributed to the involvement of melts of partly dehydrated subducted sediment and altered oceanic crust in the mantle source.

(3) During the opening of the Gulf of California, the enriched recycled compositions in the mantle source were gradually exhausted, while the contribution from the Pacific asthenosphere incrementally increased over time. This accounts for the geochemical variations in igneous rocks from the Isla San Luis volcanic center (northern Gulf) to the Guaymas Basin (central Gulf) and the Alarcón Basin (southern Gulf), reflecting the increasing maturity of oceanic spreading from north to south within this young ocean basin.

(4) In contrast to mantle plume-induced continental interior rifting and ocean basin opening, such as the Red Sea, the Guaymas Basin magmas were derived from metasomatized mantle that has undergone long-term subduction. The Guaymas Basin preserves the unique geochemical signature of the nascent oceanic crust and corroborates rapid continental margin rifting and associated ocean opening.

Declaration of Competing Interest

The authors declare that they have no known competing financial interests or personal relationships that could have appeared to influence the work reported in this paper.

Data availability

Data will be made available on request.

Acknowledgments

Appendix A. Supplementary data

Supplementary data to this article can be found online at https://doi.org/10.1016/j.chemgeo.2023.121836.

References

Aguillón-Robles, A., Calmus, T., Benoit, M., Bellon, H., Maury, R., Cotten, J., Bourgois, J., Michaud, F., 2001. Late Miocene adakites and Nb-enriched basalts from Vizcaino Peninsula, Mexico: Indicators of East Pacific rise subduction below southern Baja California? Geology 29 (6), 531–534.

Almalki, K.A., Betts, P.G., Ailleres, L., 2015. The Red Sea – 50 years of geological and geophysical research. Earth Sci. Rev. 147, 109–140.

Altherr, R., Henjes-Kunst, F., Puchelt, H., Baumann, A., 1988. Volcanic activity in the Red Sea axial trough — evidence for a large mantle diapir? Tectonophysics 150 (1), 121–133.

Altherr, R., Henjes-Kunst, F., Baumann, A., 1990. Asthenosphere versus lithosphere as possible sources for basaltic magmas erupted during formation of the Red Sea: constraints from Sr, Pb and Nd isotopes. Earth Planet. Sci. Lett. 96 (3), 269–286.

Atwater, T., Stock, J., 1998. Pacific-North America Plate Tectonics of the Neogene Southwestern United States: an Update. Int. Geol. Rev. 40 (5), 375–402.

Augustin, N., Devey, C.W., van der Zwan, F.M., Feldens, P., Tominaga, M., Bantan, R.A., Kwasnitschka, T., 2014. The rifting to spreading transition in the Red Sea. Earth Planet. Sci. Lett. 395, 217–230.

Avellán, D.R., Macías, J.L., Arce, J.L., Jiménez-Haro, A., Saucedo-Girón, R., Garduño-Monroy, V.H., Sosa-Ceballos, G., Bernal, J.P., López-Loera, H., Cisneros, G., Layer, P. W., García-Sánchez, L., Reyes-Agustín, G., Rocha, V.S., Rangel, E., 2018. Eruptive chronology and tectonic context of the late Pleistocene Tres Vírgenes volcanic complex, Baja California Sur (México). J. Volcanol. Geotherm. Res. 360, 100–125.

Bebout, G.E., Nakamura, E., 2003. Record in metamorphic tourmalines of subduction-zone devolatilization and boron cycling. Geology 31 (5), 407–410.

Bellon, H., Aguillón-Robles, A., Calmus, T., Maury, R.C., Bourgois, J., Cotten, J., 2006. La Purísima volcanic field, Baja California Sur (Mexico): Miocene to Quaternary volcanism related to subduction and opening of an asthenospheric window. J. Volcanol. Geotherm. Res. 152 (3), 253–272.

Benoit, M., Aguillón-Robles, A., Calmus, T., Maury, René C., Bellon, H., Cotten, J., Bourgois, J., Michaud, F., 2002. Geochemical Diversity of late Miocene Volcanism in Southern Baja California, Mexico: Implication of Mantle and Crustal sources during the opening of an Asthenospheric Window. J. Geol. 110 (6), 627–648.

Benton, L.D., Ryan, J.G., Tera, F., 2001. Boron isotope systematics of slab fluids as inferred from a serpentine seamount, Mariana forearc. Earth Planet. Sci. Lett. 187 (3), 273–282.

Bischoff, J.L., Pitzer, K.S., 1985. Phase relations and adiabats in boiling seafloor geothermal systems. Earth Planet. Sci. Lett. 75 (4), 327–338.

Bosworth, W., 2015. Geological evolution of the Red Sea: Historical background, review, and synthesis. In: Rasul, N.M.A., Stewart, I.C.F. (Eds.), The Red Sea: The Formation, Morphology, Oceanography and Environment of a Young Ocean Basin. Springe Berlin Heidelberg, Berlin, Heidelberg, pp. 45–78.

Busby, C., Graettinger, A., Martínez, M.L., Medynski, S., Niemi, T., Andrews, C., Bowman, E., Gutierrez, E.P., Henry, M., Lodes, E., Ojeda, J., Rice, J., Andrews, G., Brown, S., 2020. Volcanic record of the arc-to-rift transition onshore of the Guaymas Basin in the Santa Rosalía area, Gulf of California, Baja California. Geosphere 16 (4), 1012–1041.

Calmus, T., Aguillón-Robles, A., Maury, R.C., Bellon, H., Benoit, M., Cotten, J., Bourgois, J., Michaud, F., 2003. Spatial and temporal evolution of basalts and magnesian andesites ("bajaites") from Baja California, Mexico: the role of slab melts. Lithos 66 (1), 77–105.

Calmus, T., Pallares, C., Maury, R.C., Aguillon-Robles, A., Bellon, H., Benoit, M., Michaud, F., 2011. Volcanic Markers of the Post-Subduction Evolution of Baja California and Sonora, Mexico: Slab Tearing Versus Lithospheric Rupture of the Gulf of California. Pure Appl. Geophys. 168 (8–9), 1303–1330.

Castillo, P.R., 2008. Origin of the adakite–high-Nb basalt association and its implications for postsubduction magmatism in Baja California, Mexico. GSA Bull. 120 (3–4), 451–462.

Castillo, P.R., 2009. Origin of Nb-enriched basalts and adakites in Baja California, Mexico, revisited: Reply. GSA Bull. 121 (9–10), 1470–1472.

Castillo, P.R., Hawkins, J.W., Lonsdale, P.F., Hilton, D.R., Shaw, A.M., Glascock, M.D., 2002. Petrology of Alarcon Rise lavas, Gulf of California: Nascent intracontinental ocean crust. J. Geophys. Res. Solid Earth 107 (B10). ECV 5–1-ECV 5–15.

Catanzaro, E.J., Murphy, T.J., Garner, E.L., Shields, W.R., 1969. Absolute isotopic abundance ratio and atomic weight of terrestrial rubidium. J. Res. National Bureau Stand. Sec. Phys. Chem. 73a (5), 511–516.

Chu, D., Gordon, R.G., 1998. Current plate motions across the Red Sea. Geophys. J. Int. 135 (2), 313–328.

Cochran, J.R., 1983. A Model for Development of Red Sea. AAPG Bull. Am. Assoc. Pet. Geol. 67, 41–69.

Conly, A.G., Brenan, J.M., Bellon, H., Scott, S.D., 2005. Arc to rift transitional volcanism in the Santa Rosalía Region, Baja California Sur, Mexico. J. Volcanol. Geotherm. Res. 142 (3–4), 303–341.

Courtillot, V., 1982. Propagating rifts and continental breakup. Tectonics 1 (3), 239–250.

Dal Zilio, L., Faccenda, M., Capitanio, F., 2018. The role of deep subduction in supercontinent breakup. Tectonophysics 746, 312–324.

De Hoog, C.J.M., Savov, I.P., 2018. Boron isotopes as a tracer of subduction zone processes. In: Marschall, H., Foster, G. (Eds.), Boron Isotopes: The Fifth Element. Springer International Publishing, Cham, pp. 217–247.

Ebinger, C.J., Sleep, N.H., 1998. Cenozoic magmatism throughout East Africa resulting from impact of a single plume. Nature 395 (6704), 788–791.

Foster, G.L., Pogge von Strandmann, P.A.E., Rae, J.W.B., 2010. Boron and magnesium isotopic composition of seawater. Geochem. Geophys. Geosyst. 11 (8), Q08015.

Gastil, G., Krummenacher, D., Minch, J., 1979. The record of Cenozoic volcanism around the Gulf of California. GSA Bull. 90 (9), 839–857.

Girdler, R.W., 1991. The Afro-Arabian rift system—an overview. Tectonophysics 197 (2), 139–153.

Haase, K.M., Mühe, R., Stoffers, P., 2000. Magmatism during extension of the lithosphere: geochemical constraints from lavas of the Shaban deep, northern Red Sea. Chem. Geol. 166 (3), 225–239.

Hawkesworth, C.J., Gallagher, K., Hergt, J.M., McDermott, F., 1993. Mantle and Slab Contributions in ARC Magmas. Annu. Rev. Earth Planet. Sci. 21 (2), 175–204.

He, M., Xia, X., Huang, X., Ma, J., Zou, J., Yang, Q., Yang, F., Zhang, Y., Yang, Y., Wei, G., 2020. Rapid determination of the original boron isotopic composition from altered basaltic glass by in situ secondary ion mass spectrometry. J. Anal. At. Spectrom. 35 (2), 238–245.

He, P.L., Huang, X.L., Yang, F., Wang, X., 2021. Mineralogy Constraints on Magmatic Processes Controlling Adakitic Features of early Permian High-magnesium Diorites in the Western Tianshan Orogenic Belt. J. Petrol. 61 (11–12).

Henry, C.D., Aranda-Gomez, J.J., 2000. Plate interactions control middle–late Miocene, proto-Gulf and Basin and Range extension in the southern Basin and Range. Tectonophysics 318, 1–26.

Hervig, R.L., Moore, G.M., Williams, L.B., Peacock, S.M., Holloway, J.R., Roggensack, K., 2002. Isotopic and elemental partitioning of boron between hydrous fluid and silicate melt. Am. Mineral. 87 (5–6), 769–774.

Ishikawa, T., Nakamura, E., 1993. Boron isotope systematics of marine sediments. Earth Planet. Sci. Lett. 117, 567–580.

Ishikawa, T., Nakamura, E., 1994. Origin of the slab component in arc lavas from cross-arc variation of B and Pb isotopes. Nature 370 (6486), 205–208.

Ishikawa, T., Tera, F., 1999. Two isotopically distinct fluid components involved in the Mariana arc: evidence from Nb/B ratios and B, Sr, Nd, and Pb isotope systematics. Geology 27 (1), 83–86.

Izzeldin, A.Y., 1987. Seismic, gravity and magnetic surveys in the central part of the Red Sea: their interpretation and implications for the structure and evolution of the Red Sea. Tectonophysics 143 (4), 269–306.

Kelemen, P.B., Hanghøj, K., Greene, A.R., 2014. One View of the Geochemistry of Subduction-Related Magmatic Arcs, with an Emphasis on Primitive Andesite and lower Crust. In: Holland, H.D., Turekian, K.K. (Eds.), Treatise on Geochemistry, Second edition. Elsevier, Oxford, pp. 749–806.

Kent, A.J.R., Norman, M.D., Hutcheon, I.D., Stolper, E.M., 1999. Assimilation of seawater-derived components in an oceanic volcano: evidence from matrix glasses and glass inclusions from Loihi seamount, Hawaii. Chem. Geol. 156 (1), 299–319.

Kessel, R., Schmidt, M.W., Ulmer, P., Pettke, T., 2005. Trace element signature of subduction-zone fluids, melts and supercritical liquids at 120–180 km depth. Nature 437 (7059), 724–727.

Konrad-Schmolke, M., Halama, R., 2014. Combined thermodynamic–geochemical modeling in metamorphic geology: Boron as tracer of fluid–rock interaction. Lithos 208-209, 393–414.

Kowalski, P.M., Wunder, B., 2018. Boron isotope fractionation among vapor–liquids–solids–melts: experiments and atomistic modeling. In: Marschall, H., Foster, G. (Eds.), Boron Isotopes: The Fifth Element. Springer International Publishing, Cham, pp. 33–69.

Leeman, W.P., Tonarini, S., Chan, L.H., Borg, L.E., 2004. Boron and lithium isotopic variations in a hot subduction zone—the southern Washington Cascades. Chem. Geol. 212 (1), 101–124.

Li, H., Hermann, J., Zhang, L., 2022. Melting of subducted slab dictates trace element recycling in global arcs. Sci. Adv. 8 (2), eabh2166.

Ligi, M., Bonatti, E., Rasul, N.M.A., 2015. Seafloor spreading initiation: Geophysical and geochemical constraints from the Thetis and Nereus Deeps, Central Red Sea. In: Rasul, N.M.A., Stewart, I.C.F. (Eds.), The Red Sea: The Formation, Morphology, Oceanography and Environment of a Young Ocean Basin. Springer, Berlin Heidelberg, Berlin, Heidelberg, pp. 79–98.

Ligi, M., Bonatti, E., Bosworth, W., Cai, Y., Cipriani, A., Palmiotto, C., Ronca, S., Seyler, M., 2018. Birth of an ocean in the Red Sea: Oceanic-type basaltic melt intrusions precede continental rupture. Gondwana Res. 54, 150–160.

Liu, M., Gerya, T., Rozel, A.B., 2022. Self-organization of magma supply controls crustal thickness variation and tectonic pattern along melt-poor mid-ocean ridges. Earth Planet. Sci. Lett. 584, 117482.

Lizarralde, D., Axen, G.J., Brown, H.E., Fletcher, J.M., Gonzalez-Fernandez, A., Harding, A.J., Holbrook, W.S., Kent, G.M., Paramo, P., Sutherland, F., Umhoefer, P. J., 2007. Variation in styles of rifting in the Gulf of California. Nature 448 (7152), 466–469.

Marschall, H.R., Altherr, R., Rüpke, L., 2007. Squeezing out the slab — modelling the release of Li, Be and B during progressive high-pressure metamorphism. Chem. Geol. 239 (3), 323–335.

Marschall, H.R., Wanless, V.D., Shimizu, N., von Strandmann, P.A.E.P., Elliott, T., Monteleone, B.D., 2017. The boron and lithium isotopic composition of mid-ocean ridge basalts and the mantle. Geochim. Cosmochim. Acta 207, 102–138.

Martín-Barajas, A., Stock, J.M., Layer, P., Hausback, B., Renne, P., López-Martínez, M., 1995. Arc-rift transition volcanism in the Puertecitos Volcanic Province, northeastern Baja California, Mexico. GSA Bull. 107 (4), 407–424.

Maury, R.C., Calmus, T., Pallares, C., Benoit, M., Grégoire, M., Aguillón-Robles, A., Bellon, H., Bohn, M., 2009. Origin of the adakite–high-Nb basalt association and its implications for postsubduction magmatism in Baja California, Mexico: Discussion. GSA Bull. 121 (9–10), 1465–1469.

Mcdonough, W.F., Sun, S.S., 1995. The composition of the Earth. Chem. Geol. 120, 223–253.

Michael, P.J., Schilling, J.-G., 1989. Chlorine in mid-ocean ridge magmas: evidence for assimilation of seawater-influenced components. Geochim. Cosmochim. Acta 53, 3131–3143.

Michaud, F., Royer, J.Y., Bourgois, J., Dyment, J., Calmus, T., Bandy, W., Sosson, M., Mortera-Gutiérrez, C., Sichler, B., Rebolledo-Viera, M., Pontoise, B., 2006. Oceanic-ridge subduction vs. slab break off: Plate tectonic evolution along the Baja California Sur continental margin since 15 Ma. Geology 34 (1), 13–16.

Miller, N.C., Lizarralde, D., 2013. Thick evaporites and early rifting in the Guaymas Basin, Gulf of California. Geology 41 (2), 283–286.

Mora-Klepeis, G., McDowell, F.W., 2004. Late Miocene calc-alkalic volcanism in northwestern Mexico: evidence of rift or subduction-related magmatism? J. S. Am. Earth Sci. 17 (4), 297–310.

Morgan, J.P., Chen, Y.J., 1993. Dependence of ridge-axis morphology on magma supply and spreading rate. Nature 364 (6439), 706–708.

Nauret, F., Hémond, C., Maury, R.C., Aguillon-Robles, A., Guillou, H., Le Faouder, A., 2012. Extreme ^{230}Th excesses in magnesian andesites from Baja California. Lithos 146-147, 143–151.

Ni, H., Zhang, L., Xiong, X., Mao, Z., Wang, J., 2017. Supercritical fluids at subduction zones: evidence, formation condition, and physicochemical properties. Earth Sci. Rev. 167, 62–71.

Niu, Y., O'Hara, M.J., 2003. Origin of ocean island basalts: a new perspective from petrology, geochemistry, and mineral physics considerations. J. Geophys. Res. Solid Earth 108 (B4), 2209.

Oskin, M., Stock, J., 2003. Marine incursion synchronous with plate-boundary localization in the Gulf of California. Geology 31 (1), 23–26.

Oskin, M., Stock, J., Martín-Barajas, A., 2001. Rapid localization of Pacific–North America plate motion in the Gulf of California. Geology 29 (5), 459–462.

Pabst, S., Zack, T., Savov, I.P., Ludwig, T., Rost, D., Tonarini, S., Vicenzi, E.P., 2012. The fate of subducted oceanic slabs in the shallow mantle: Insights from boron isotopes and light element composition of metasomatized blueschists from the Mariana forearc. Lithos 132-133, 162–179.

Pallares, C., Maury, R.C., Bellon, H., Royer, J.-Y., Calmus, T., Aguillón-Robles, A., Cotten, J., Benoit, M., Michaud, F., Bourgois, J., 2007. Slab-tearing following ridge-trench collision: evidence from Miocene volcanism in Baja California, México. J. Volcanol. Geotherm. Res. 161 (1–2), 95–117.

Pallares, C., Bellon, H., Benoit, M., Maury, R.C., Aguillón-Robles, A., Calmus, T., Cotten, J., 2008. Temporal geochemical evolution of Neogene volcanism in northern Baja California (27°–30° N): Insights on the origin of post-subduction magnesian andesites. Lithos 105 (1–2), 162–180.

Paz Moreno, F.A., Demant, A., 1999. The recent Isla San Luis volcanic Centre: petrology of a rift-related volcanic suite in the northern Gulf of California, Mexico. J. Volcanol. Geotherm. Res. 93 (1), 31–52.

Pearce, J.A., 2008. Geochemical fingerprinting of oceanic basalts with applications to ophiolite classification and the search for Archean oceanic crust. Lithos 100 (1–4), 14–48.

Plank, T., 2014. The chemical composition of subducting sediments. In: Holland, H.D., Turekian, K.K. (Eds.), Treatise on Geochemistry, Second edition. Elsevier, Oxford, pp. 607–629.

Plank, T., Langmuir, C.H., 1998. The chemical composition of subducting sediment and its consequences for the crust and mantle. Chem. Geol. 145 (3), 325–394.

Plattner, C., Malservisi, R., Dixon, T.H., LaFemina, P., Sella, G.F., Fletcher, J., Suarez-Vidal, F., 2007. New constraints on relative motion between the Pacific Plate and Baja California microplate (Mexico) from GPS measurements. Geophys. J. Int. 170 (3), 1373–1380.

Prause, S., Weisenberger, T.B., Kleine, B.I., Monien, P., Rispoli, C., Stefánsson, A., 2022. Alteration of basaltic glass within the Surtsey hydrothermal system, Iceland – Implication to oceanic crust seawater interaction. J. Volcanol. Geotherm. Res. 429, 107581.

Reekie, C.D.J., Jenner, F.E., Smythe, D.J., Hauri, E.H., Bullock, E.S., Williams, H.M., 2019. Sulfide resorption during crustal ascent and degassing of oceanic plateau basalts. Nat. Commun. 10 (82), 1–11.

Rogers, G., Saunders, A.D., 1989. Magnesian andesites from Mexico, Chile and the Aleutian Islands: Implications for magmatism associated with ridge-trench collision. In: Crawford, A.J. (Ed.), Boninites. Unwin-Hyman, London, pp. 416–445.

Rogers, G., Saunders, A.D., Terrell, D.J., Verma, S.P., Marriner, G.F., 1985. Geochemistry of Holocene volcanic rocks associated with ridge subduction in Baja California, Mexico. Nature 315 (6018), 389–392.

Rudnick, R.L., Gao, S., 2014. Composition of the continental crust. In: Holland, H.D., Turekian, K.K. (Eds.), Treatise on Geochemistry, Second edition. Elsevier, Oxford, pp. 1–51.

Rustioni, G., Audetat, A., Keppler, H., 2021. The composition of subduction zone fluids and the origin of the trace element enrichment in arc magmas. Contrib. Mineral. Petrol. 176 (51), 1–19.

Ryan, J.G., Leeman, W.P., Morris, J.D., Langmuir, C.H., 1996. The boron systematics of intraplate lavas: Implications for crust and mantle evolution. Geochim. Cosmochim. Acta 60 (3), 415–422.

Ryan, W.B.F., Carbotte, S.M., Coplan, J.O., O'Hara, S., Melkonian, A., Arko, R., Weissel, R.A., Ferrini, V., Goodwillie, A., Nitsche, F., Bonczkowski, J., Zemsky, R., 2009. Global Multi-Resolution Topography synthesis. Geochem. Geophys. Geosyst. 10 (3), Q03014.

Salters, V.J.M., Stracke, A., 2004. Composition of the depleted mantle. Geochem. Geophys. Geosyst. 5 (5), Q05B07.

Sanfilippo, A., Salters, V.J.M., Sokolov, S.Y., Peyve, A.A., Stracke, A., 2021. Ancient refractory asthenosphere revealed by mantle re-melting at the Arctic Mid Atlantic Ridge. Earth Planet. Sci. Lett. 566, 116981.

Saunders, A.D., Fornari, D.J., Joron, J.-L., Tarney, J., Treuil, M., 1982a. Geochemistry of basic igneous rocks, Gulf of California, Deep Sea Drilling Project Leg. 64. In: Blaklee, J., Platt, L.W., Stout, L.N. (Eds.), Initial Reports of Deep Sea Drilling Project, Washington, pp. 595–642.

Saunders, A.D., Fornari, D.J., Morrison, M.A., 1982b. The composition and emplacement of basaltic magmas produced during the development of continental-margin basins: the Gulf of California, Mexico. J. Geol. Soc. 139 (3), 335.

Saunders, A.D., Rogers, G., Marriner, G.F., Terrell, D.J., Verma, S.P., 1987. Geochemistry of Cenezoic volcanic rocks, Baja California, Mexico: Implications for the petrogenesis of post-subduction magmas. J. Volcanol. Geotherm. Res. 32 (1), 223–245.

Scambelluri, M., Müntener, O., Ottolini, L., Pettke, T.T., Vannucci, R., 2004. The fate of B, Cl and Li in the subducted oceanic mantle and in the antigorite breakdown fluids. Earth Planet. Sci. Lett. 222 (1), 217–234.

Schmid, C., Goes, S., van der Lee, S., Giardini, D., 2002. Fate of the Cenozoic Farallon slab from a comparison of kinematic thermal modeling with tomographic images. Earth Planet. Sci. Lett. 204 (1), 17–32.

Schmidt, M.W., Jagoutz, O., 2017. The global systematics of primitive arc melts. Geochem. Geophys. Geosyst. 18 (8), 2817–2854.

Shaw, A.M., Hauri, E.H., Behn, M.D., Hilton, D.R., Macpherson, C.G., Sinton, J.M., 2012. Long-term preservation of slab signatures in the mantle inferred from hydrogen isotopes. Nat. Geosci. 5 (3), 224–228.

Shimizu, K., Saal, A.E., Myers, C.E., Nagle, A.N., Hauri, E.H., Forsyth, D.W., Kamenetsky, V.S., Niu, Y., 2016. Two-component mantle melting-mixing model for the generation of mid-ocean ridge basalts: Implications for the volatile content of the Pacific upper mantle. Geochim. Cosmochim. Acta 176, 44–80.

Sigloch, K., 2011. Mantle provinces under North America from multifrequency P wave tomography. Geochem. Geophys. Geosyst. 12 (2), Q02W08.

Smith, A.D., 1999. The Nd-Sr-Pb Isotopic Record in Abyssal Tholeiites from the Gulf of California Region, Western Mexico: no evidence for a Gulf Mouth Plume. Int. Geol. Rev. 41 (10), 921–931.

Spivack, A.J., Edmond, J.M., 1987. Boron isotope exchange between seawater and the oceanic crust. Geochim. Cosmochim. Acta 51 (5), 1033–1043.

Stock, J.M., Hodges, K.V., 1989. Pre-Pliocene Extension around the Gulf of California and the transfer of Baja California to the Pacific Plate. Tectonics 8 (1), 99–115.

Sun, S.S., McDonough, W.F., 1989. Chemical and isotopic systematics of oceanic basalts: implications for mantle composition and processes. Geol. Soc. Lond. Spec. Publ. 42, 313–345.

Sun, W.D., Binns, R.A., Fan, A.C., Kamenetsky, V.S., Wysoczanski, R., Wei, G.J., Hu, Y.H., Arculus, R.J., 2007. Chlorine in submarine volcanic glasses from the eastern Manus basin. Geochim. Cosmochim. Acta 71 (6), 1542–1552.

Teske, A., McKay, L.J., Ravelo, A.C., Aiello, I., Mortera, C., Núñez-Useche, F., Canet, C., Chanton, J.P., Brunner, B., Hensen, C., Ramírez, G.A., Sibert, R.J., Turner, T., White, D., Chambers, C.R., Buckley, A., Joye, S.B., Soule, S.A., Lizarralde, D., 2019. Characteristics and Evolution of sill-driven off-axis hydrothermalism in Guaymas Basin – the Ringvent site. Sci. Rep. 9 (1), 13847.

Teske, A., Lizarralde, D., Höfig, T.W., Aiello, I.W., Ash, J.L., Bojanova, D.P., Buatier, M. D., Edgcomb, V.P., Galerne, C.Y., Gontharet, S., Heuer, V.B., Jiang, S., Kars, M.A.C., Khogenkumar Singh, S., Kim, J., Koornneef, L.M.T., Marsaglia, K.M., Meyer, N.R., Morono, Y., Negrete-Aranda, R., Neumann, F., Pastor, L.C., Peña-Salinas, M.E., Pérez Cruz, L.L., Ran, L., Riboulleau, A., Sarao, J.A., Schubert, F., Stock, J.M., Toffin, L.M. A.A., Xie, W., Yamanaka, T., Zhuang, G., 2021. Expedition 385 summary. In: Teske, A., Lizarralde, D., Höfig, T.W., Expedition 385 Scientists (Eds.), Proceedings of the International Ocean Discovery Program, 385. International Ocean Discovery Program), College Station, TX.

Tonarini, S., Agostini, S., Doglioni, C., Innocenti, F., Manetti, P., 2007. Evidence for serpentinite fluid in convergent margin systems: the example of El Salvador (Central America) arc lavas. Geochem. Geophys. Geosyst. 8 (9), Q09014.

Umhoefer, P.J., 2011. Why did the Southern Gulf of California rupture so rapidly?— Oblique divergence across hot, weak lithosphere along a tectonically active margin. GSA Today 21 (11), 4–10.

van der Zwan, F.M., Devey, C.W., Augustin, N., Almeev, R.R., Bantan, R.A., Basaham, A., 2015. Hydrothermal activity at the ultraslow- to slow-spreading Red Sea Rift traced by chlorine in basalt. Chem. Geol. 405, 63–81.

Velderrain-Rojas, L.A., Vidal-Solano, J.R., 2023. Middle-late Miocene rift-related magmatism in Guaymas, Sonora, Mexico at the eastern margin of the Gulf of California: Petrogenetic implications associated to the Pacific-north American plate boundary. Appl. Geochem. 148, 105508.

Verma, S.P., 1983. Strontium and neodymium isotope geochemistry of igneous rocks from the North East Pacific and Gulf of California. Chem. Geol. 41, 339–356.

Vidal-Solano, J.R., Demant, A., Paz Moreno, F.A., Lapierre, H., Ortega-Rivera, M.A., Lee, J.K.W., 2008. Insights into the tectonomagmatic evolution of NW Mexico: Geochronology and geochemistry of the Miocene volcanic rocks from the Pinacate area, Sonora. GSA Bull. 120 (5–6), 691–708.

White, W.W., Klein, E.M., 2014. Composition of the Oceanic Crust. In: Holland, H.D., Turekian, K.K. (Eds.), Treatise on Geochemistry, Second edition. Elsevier, Oxford, pp. 457–496.

Wilson, J.T., 1966. Did the Atlantic close and then re-open? Nature 211 (5050), 676–681.

Wilson, R.W., Houseman, G.A., Buiter, S.J.H., McCaffrey, K.J.W., Doré, A.G., 2019. Fifty years of the Wilson Cycle concept in plate tectonics: an overview. Geol. Soc. Lond. Spec. Publ. 470 (1), 1–17.

Yang, A.Y., Langmuir, C.H., Cai, Y., Michael, P., Goldstein, S.L., Chen, Z., 2021. A subduction influence on ocean ridge basalts outside the Pacific subduction shield. Nat. Commun. 12 (1), 4757.

Yu, Y., Huang, X.-L., Sun, M., Ma, J.-L., 2021. B isotopic constraints on the role of H_2O in mantle wedge melting. Geochim. Cosmochim. Acta 303, 92–109.

Zhang, X., Paulssen, H., Lebedev, S., Meier, T., 2009. 3D shear velocity structure beneath the Gulf of California from Rayleigh wave dispersion. Earth Planet. Sci. Lett. 279 (3), 255–262.

Zhang, C., Wang, L.X., Marks, M.A.W., France, L., Koepke, J., 2017. Volatiles (CO_2, S, F, Cl, Br) in the dike-gabbro transition zone at IODP Hole 1256D: Magmatic imprint versus hydrothermal influence at fast-spreading mid-ocean ridge. Chem. Geol. 459, 43–60.

Zhang, L., Ren, Z.Y., Wu, Y.D., Li, N., 2018. Strontium isotope measurement of basaltic glass by laser ablation multiple collector inductively coupled plasma mass spectrometry based on a linear relationship between analytical bias and Rb/Sr ratios. Rapid Commun. Mass Spectrom. 32 (2), 105–112.

Zhang, L., Ren, Z.Y., Xia, X.P., Yang, Q., Hong, L.B., Wu, D., 2019. In situ determination of trace elements in melt inclusions using laser ablation inductively coupled plasma sector field mass spectrometry. Rapid Commun. Mass Spectrom. 33 (4), 361–370.